Cluster Difference Imaging Photometric Survey. Vetting Report Description Document

L. G. BOUMA,[1] J. D. HARTMAN,[1] W. BHATTI,[1] J. N. WINN,[1] AND G. Á. BAKOS[1]

[1] *Department of Astrophysical Sciences, Princeton University, 4 Ivy Lane, Princeton, NJ 08540, USA*

ABSTRACT

To find planet candidates in clusters, we make vetting reports using our light-curves (Bouma et al. 2019) and auxiliary data. This document describes the CDIPS planet candidate vetting reports uploaded by `bouma` to ExoFOP-TESS 2020-01-20 through 2020-05-01. Earlier versions of this document are available at lgbouma.com/notes.

1. VETTING REPORT DESCRIPTION

The NASA team and MIT teams (Jenkins et al. 2010; Huang et al. 2018) produce vetting reports to assess the quality of planet candidates identified through their transiting planet serach pipelines.

One goal of the CDIPS project is to detect transiting planets with known ages. Therefore our vetting reports include information to help assess *(a)* whether the transiting planet candidate is real, and *(b)* whether the reported age is correct. The code used to make these reports is available online[1].

Figures 1 to 7 summarize the document construed for these purposes. The planet candidate chosen for these figures (Gaia-DR2 `3050033749239975552` = TIC `125192758`) was chosen because it showcases many of the vetting report features, in this case for a neighboring eclipsing binary.

1.1. *Transit search summary*

Figure 1. Periodograms from TLS and phase-dispersion minimization, calculated with `astrobase.periodbase`, are shown in the top left and top center (Bhatti et al. 2018; Hippke & Heller 2019; Stellingwerf 1978). The top three peaks from each method are shown in the second and third rows; the raw light-curve is in the top-right. A finder chart is inset to the top left, with the 1.5-pixel radius aperture used to extract the light-curve in orange. The finder charts are from The Second Digitized Sky Survey (Red); they are pulled from NASA's `skyview` service[2].

1.2. *Light-curve diagnostics*

Figure 2. Time-series of raw flux (`IRM2`), TFA-detrended flux (`TF2`), stellar-variability "detrended flux", and the background are shown as a function of barycentric Julian date. The overplotted dashed vertical lines are the ephemeris of the

highest-power TLS peak from Figure 1. An important visual check is whether the flux dips are correlated with changes in the background level – in this case, they are not. The standard deviation and TESS magnitude are quoted in the upper right. The red line in the top plot is a spline fit, which in this case helped in finding the eclipse signal.

The spline is an optional feature: it is only fitted and removed if the star is found to be "variable" (the Lomb-Scargle peak period is found with false alarm probability below 10^{-5}, within the TFA light-curves). The spline is a robust penalized B-spline, which is a B-spline with knot-length automatically determined via cross-validation (Eilers & Marx 1996). The idea behind the cross-validation is that more knots leads to smaller residuals on training data, but larger errors when tested on the entire dataset. We used the `wotan` implementation[3], which is a wrapper to the `pyGAM` spline fitter, with 2σ clipping of outliers from the fit residuals at each iteration (Servén et al. 2018; Hippke et al. 2019). The maximum number of spline knots was set to 50, which for each TESS sector (≈ 25 days) is commensurate with a ≈ 0.5 day window.

Whenever the TFA light-curve is found to be variable, the "stellar variability detrended flux" is the result of dividing the raw `IRM2` flux by the best-fit spline[4]. This is the light-curve that is then searched for transiting planets, and used in *e.g.*, Figure 1 and Figure 3. If the TFA light-curve is not found to be variable, then the `TFA2` light-curve is used for this purpose.

1.3. *Transit diagnostics*

Figure 3. The plots show the maximally-detrended light-curve (top); the phase-folded light-curve centered over ± 3 transit durations of the primary transit (middle left); the secondary eclipse (middle right); the odd-numbered transits

Corresponding author: L. G. Bouma
luke@astro.princeton.edu

---

[1] https://github.com/lgbouma/cdips/tree/57274b

[2] See https://skyview.gsfc.nasa.gov/current/cgi/survey.pl and http://archive.stsci.edu/dss/acknowledging.html

[3] We use `wotan` versions greater than `1.4`. Before `2020-03-01`, an earlier version was used, which led to qualitatively worse detrending performance for a subset of light-curves due to a floating point truncation error. See https://github.com/hippke/wotan/issues/51.

[4] Before `2020-03-01`, this definition was different. For the initial single-sector processing of S6-S11, it was the result of dividing the `TFA2` flux by the best-fit spline.

(lower left); and the even-numbered transits (lower right). Also shown is the best-fit TLS template model — by default, this assumes a non-grazing geometry (see Hippke & Heller 2019).

The stellar parameters ($T_{\rm eff}, R_\star, M_\star$) are taken from TICv8 when available (Stassun et al. 2019). For the stellar radius, if TICv8 does not quote a radius, neither will the vetting report. If TICv8 gives a stellar radius, but does not give a stellar mass, we interpolate the mass using the radius and the Pecaut & Mamajek (2013) table, under the assumption that the star is a dwarf. The effective temperatures calculated by TICv8 were estimated from an empirical color relation involving Gaia $G_{\rm Bp}$ and $G_{\rm Rp}$ magnitudes. These observed colors were dereddened first, using Pan-STARRS dust maps (Green et al. 2018) for declinations above $-30°$, and the Schlegel et al. (1998) maps otherwise.

The first eight lines of text are parameters determined from the best-fitting TLS model. The one exception is the planet radius, which uses the stellar radius as noted above. The "flux contamination" (TICCONT) from neighboring stars is *never* taken into account, because transit depth dilution does not affect image subtraction analyses in the same manner as aperture-photometry reductions. The significance of the odd-to-even asymmetry is quoted, but given the strong rotational variability in this object (Figure 2), the apparent odd-even asymmetry could have been caused by the detrending process. To estimate the transit to occultation depth ratio $\delta_{\rm tra}/\delta_{\rm occ}$, the phase-folded light-curve is also fit by a sum of two gaussians (in this case, the fit failed). "AstExc" refers to the Gaia-DR2 astrometric excess, which can indicate hints of astrometric binarity in the system. "$d_{\rm geom}$" is the geometric distance from Bailer-Jones et al. (2018). "$R_\star + M_\star \rightarrow T_{b0}$" gives the duration of a zero-eccentricity central transit based on the TICv8 stellar radius and masses discussed above.

1.4. *Light-curves for increasing aperture sizes*

Figure 4. Apertures of radius 1, 1.5, and 2.25 pixels are shown in maximally detrended light-curves from top to bottom. The blue line is the reference transit depth from the best-fitting TLS model. Changes in depth with increasing aperture size can indicate that the source of variability is off-center from the aperture, suggesting a photometric blend.

1.5. *Cluster membership assessment diagnostics*

Figure 5. The star was considered a candidate cluster member by the source(s) listed under "Reference", in this case Cantat-Gaudin et al. (2018). The name used in their catalog was in this case a Gaia-DR2 identifier, which can be back-referenced to find the membership probability they assigned this star for being in NGC 2323. The base catalog however for this page of plots is Kharchenko et al. (2013), due to its homogeneous parameter determination procedure (particularly for age). If a match to the Kharchenko et al. (2013) catalog is found, then the subplots on this page are populated; otherwise, they are not. Top-left shows the parallax, with orange points sampled from the Gaia-DR2 posterior, black points the other cluster members in the *Kharchenko cata-*

log (not the catalog claiming membership), and the blue line the claimed Kharchenko parallax for the cluster. A number of field contaminants in the Kharchenko catalog are visible in this case. Top-right are the Gaia proper motions, where against black points are cluster members from Kharchenko, and the orange is the target star. Bottom-left is the color-magnitude diagram, and bottom-right are the on-sky positions. In the text, N1sr2 is the number of 1σ cluster members reported by Kharchenko et al. (2013) within the cluster angular radius; $\log t$ is the base-10 logarithm of the age in years; type matches the type codes provided by Kharchenko et al. (2013); "Note" gives the description of the cluster from Kharchenko et al. (2013), if any is available. Extra caution must be taken when interpreting this set of plots, since they can only show disagreement between the observed star's properties and those of the listed Kharchenko members (and the latter is in some cases incomplete or otherwise biased).

1.6. *Imaging variability diagnostics*

Figure 6. This page helps diagnose which stars are producing the observed variability. Top-left and top-center are the mean out-of-transit (OOT) and mean in-transit calibrated images (created separately from our image-subtraction analysis, using TESScut, Brasseur et al. 2019). The OOT images are based on the same number of exposures as the in-transit images and split evenly before and after each transit (following Bryson et al. 2013; Kostov et al. 2019). The yellow star is the target's position from TICv8; small red crosses are WCS-projected locations of neighbor stars.

Middle-left is the most important sub-panel: the difference between the OOT and in-transit mean images. If the variability shown in the background map (units: ADU) is off-target, the signal is not from the target star. A two dimensional gaussian is fit to the inner 8x8 pixels to estimate the centroid position — the resulting best-fit location is shown as a white star, and the separation to the catalog star's position (yellow star) is labelled ctlg - gauss(OOT-intra) on the right. A different approach, simply taking the first moment of the middle-left image, gives the ctlg - <OOT-intra> line.

Middle-center is the same as middle-left, but normalized by the uncertainty map. Lower left and lower center show the DSS2-Red field in linear and log scales at roughly the same pixel scale as the TESS image, with the 1, 1.5, and 2.25 pixel-radius apertures in blue, orange, and green respectively. The brightness of neighborhood stars is given on the far right. Note the slight coordinate rotation difference between DSS and TESS images; DSS images are aligned north-up, east-left; TESS images are oriented as closely as possible to this system without actually performing the rotation.

1.7. *Neighborhood plots*

Figure 7. The analysis in Figure 5 is helpful but insufficient for determination of cluster membership. A more thorough approach is to query Gaia-DR2 for nearby stars in position, parallax, and proper motion space, and let the data speak for

itself regarding *(a)* the existence of the group, and *(b)* the target star's membership within the group.

For these plots, the "neighborhood" is defined as a group of at most 10^4 randomly selected stars within:

$$\langle \alpha \rangle \pm 5\sigma_\alpha, \qquad (1)$$

$$\langle \delta \rangle \pm 5\sigma_\delta, \qquad (2)$$

$$\langle \pi \rangle \pm 5\sigma_\pi, \qquad (3)$$

where (α, δ, π) are the right ascension, declination, and parallax. $\langle x \rangle$ denotes the mean over all stars within the claimed cluster, σ_x denotes the standard deviation. The limiting G magnitude for the "neighborhood" is set to 18 for Cantat-Gaudin et al. (2018) groups, and 16 for Kharchenko et al. (2013) groups.

The cluster members (black points) and the neighborhood members (gray points) are *mutually exclusive sets*. After the stars are randomly selected from the volume described above, any overlapping stars between the group and the neighborhood samples are removed from the neighborhood sample.

Figure 7 shows the labeled quantities from the target star, the neighborhood, and the "cluster members" reported by Cantat-Gaudin et al. (2018), Kounkel & Covey (2019), or Kharchenko et al. (2013). The top three subplots intentionally omit the labelled cluster members, in order to give the user their own by-eye assessment of whether they see clusters in the neighborhood (as might happen if the membership labelling is *incomplete*), and whether the target star is within those clusters. The middle three subplots overplot cluster members from the reference noted in the legend. The radial velocity plots (bottom row) use radial velocities from Gaia-DR2, and so are limited to roughly 3500-7000 K, for $G \lesssim 12.5$ (Katz et al. 2019).
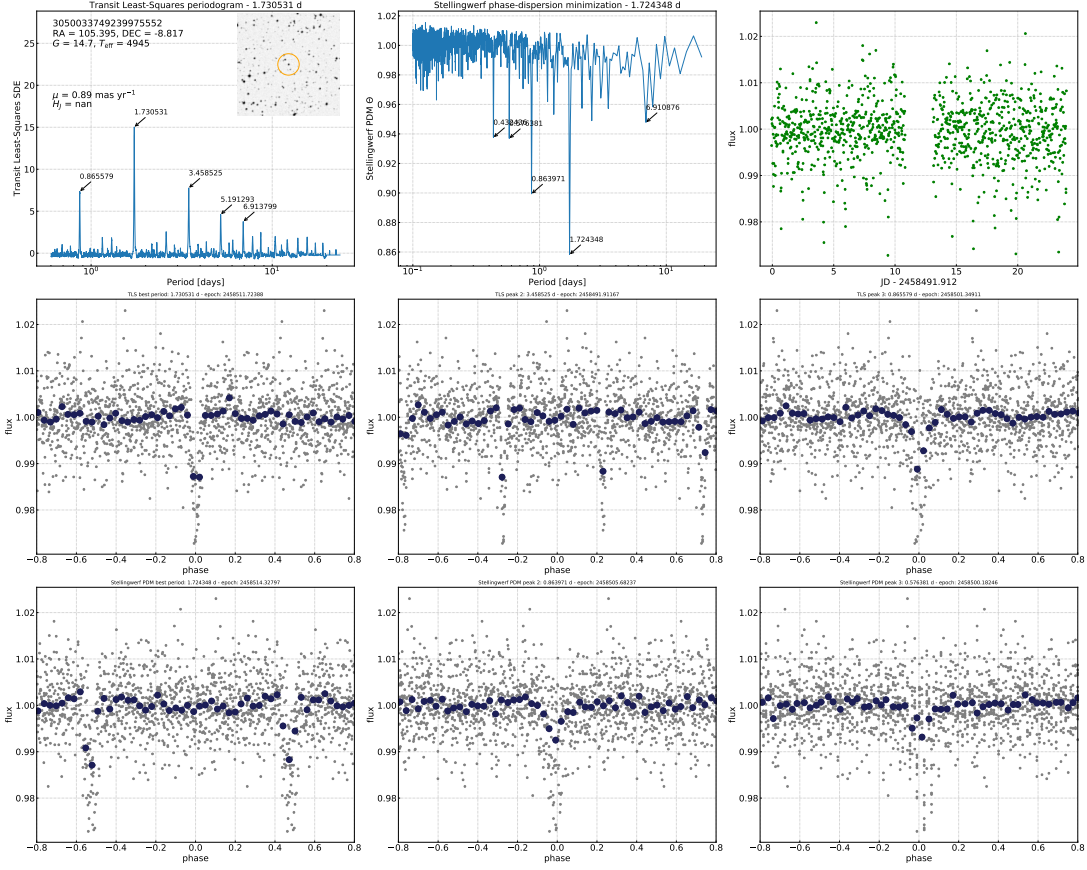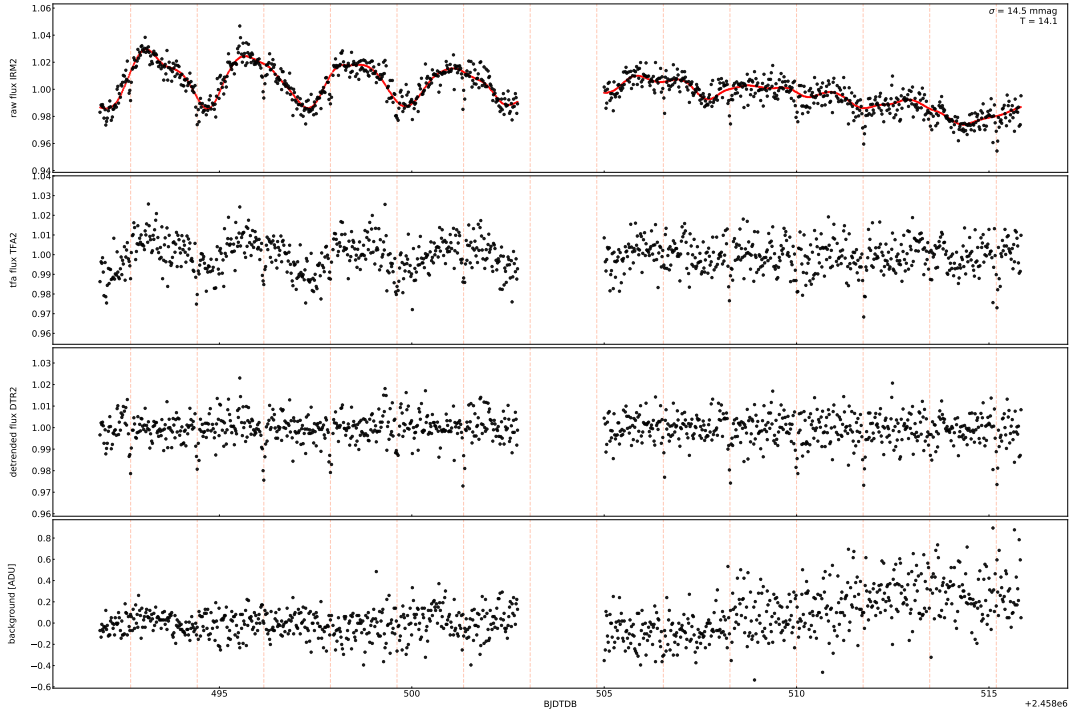
Figure 1. Transit search summary. See § 1.1.
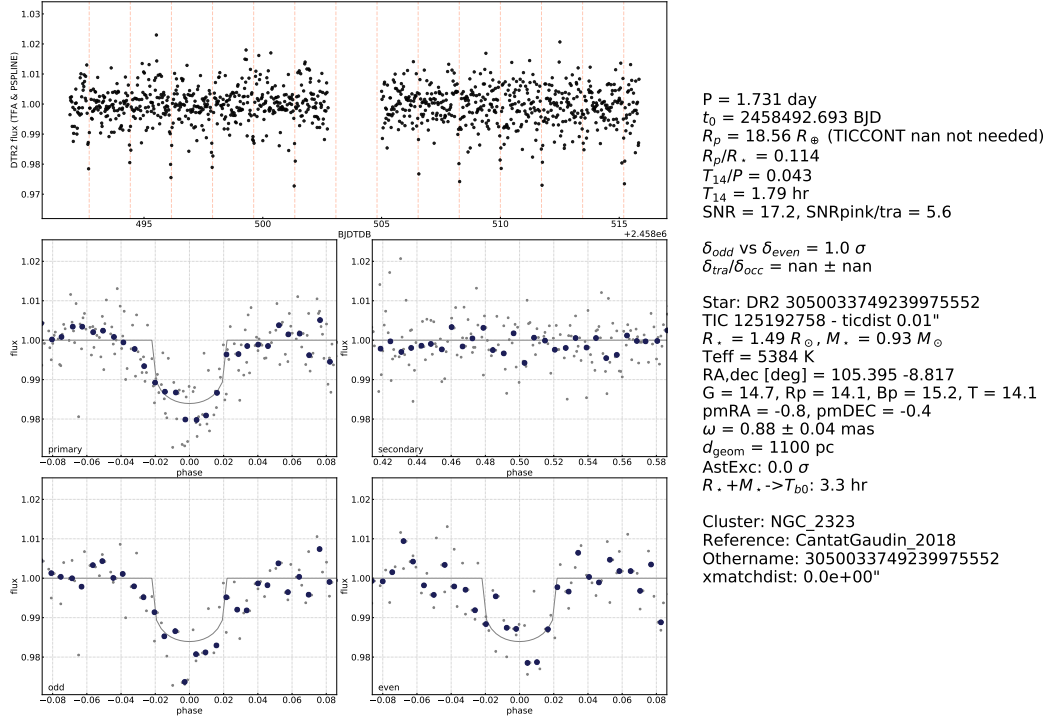

Figure 2. Light-curve diagnostics. See § 1.2.

P = 1.731 day
t_0 = 2458492.693 BJD
R_p = 18.56 $R_\oplus$ (TICCONT nan not needed)
$R_p/R_\star$ = 0.114
T_{14}/P = 0.043
T_{14} = 1.79 hr
SNR = 17.2, SNRpink/tra = 5.6

δ_{odd} vs δ_{even} = 1.0 σ
$\delta_{tra}/\delta_{occ}$ = nan ± nan

Star: DR2 3050033749239975552
TIC 125192758 - ticdist 0.01"
$R_\star$ = 1.49 $R_\odot$, $M_\star$ = 0.93 $M_\odot$
Teff = 5384 K
RA,dec [deg] = 105.395 -8.817
G = 14.7, Rp = 14.1, Bp = 15.2, T = 14.1
pmRA = -0.8, pmDEC = -0.4
ω = 0.88 ± 0.04 mas
d_{geom} = 1100 pc
AstExc: 0.0 σ
$R_\star + M_\star ->T_{b0}$: 3.3 hr

Cluster: NGC_2323
Reference: CantatGaudin_2018
Othername: 3050033749239975552
xmatchdist: 0.0e+00"

Figure 3. Transit diagnostics. See § 1.3.
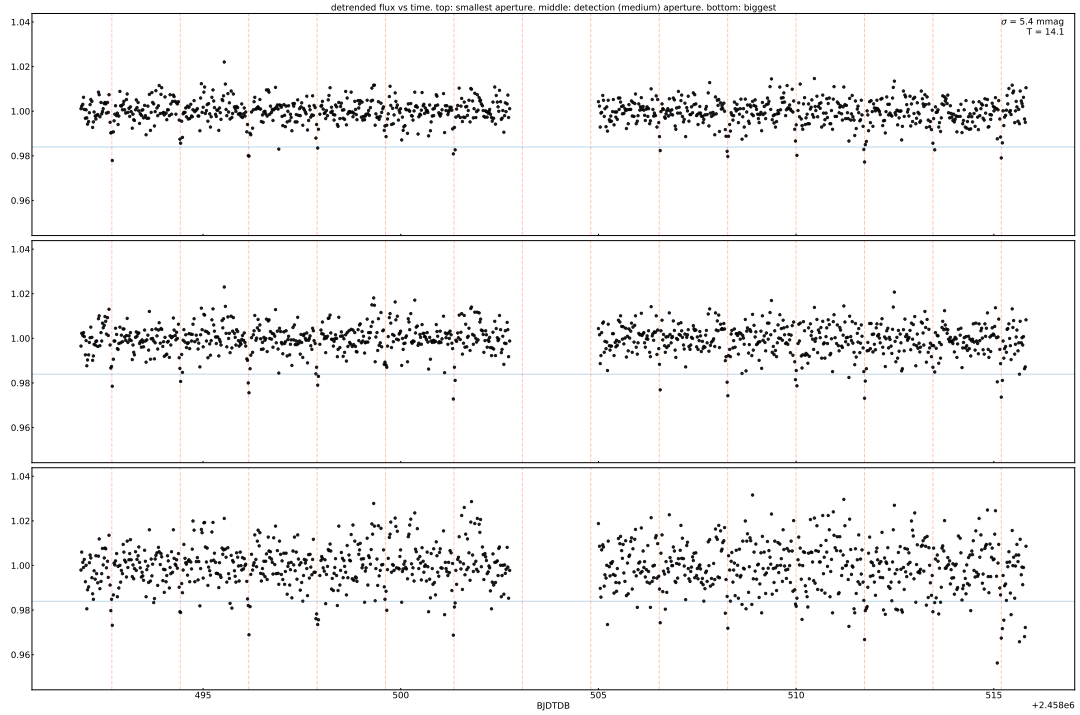
Figure 4. Light-curves for increasing aperture sizes. See § 1.4.

Figure 5. Cluster membership assessment diagnostics. See § 1.5.
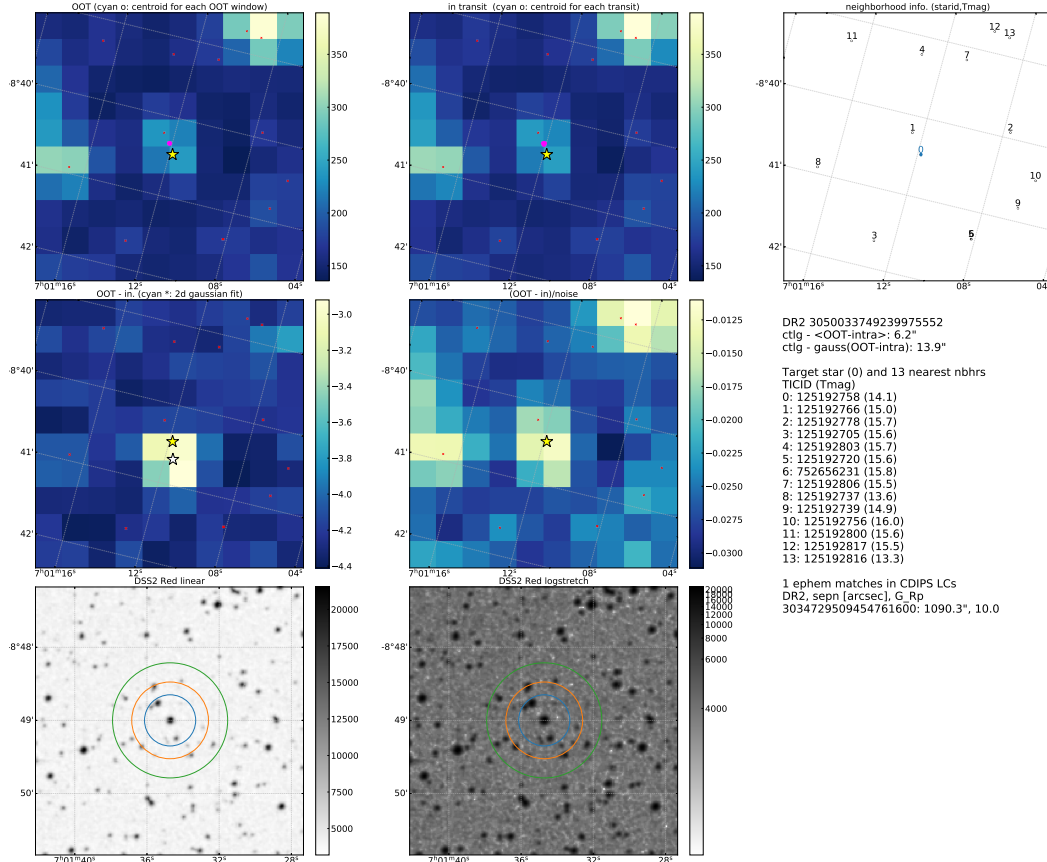

Figure 6. Imaging variability diagnostics. See § 1.6.
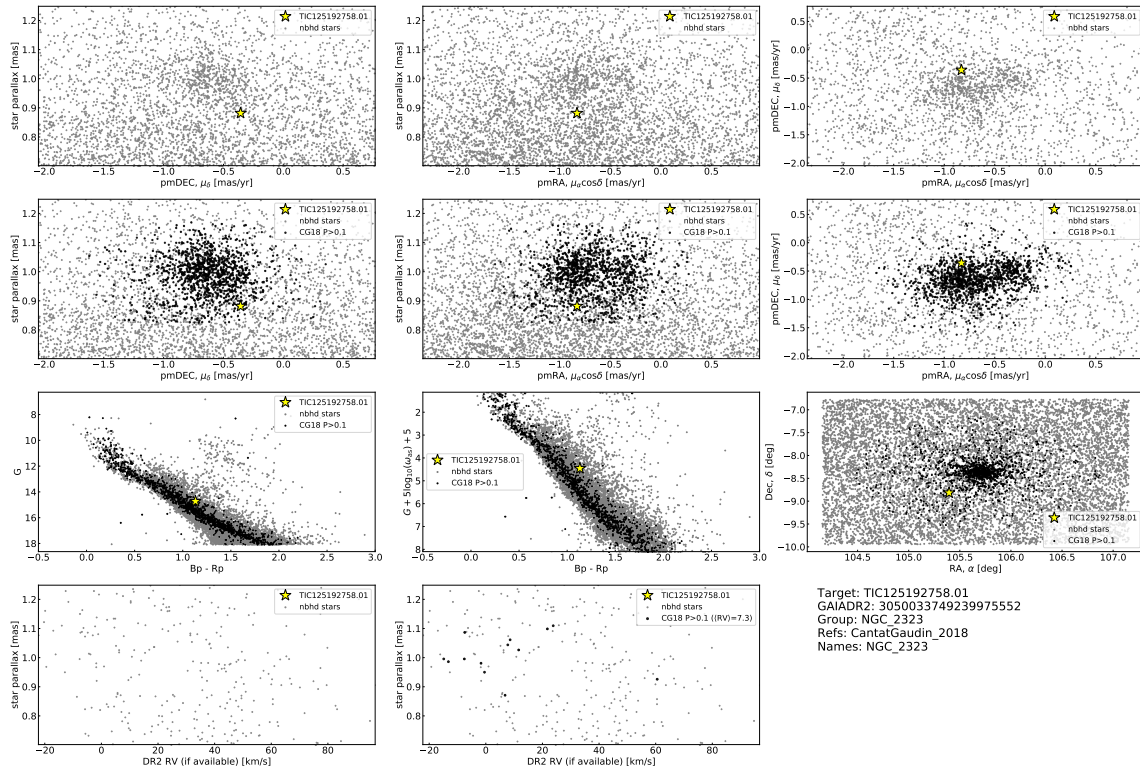
Figure 7. Neighborhood diagnostic. See § 1.7.

REFERENCES

Bailer-Jones, C. A. L., Rybizki, J., Fouesneau, M., Mantelet, G., & Andrae, R. 2018, arXiv:1804.10121 [astro-ph], arXiv: 1804.10121

Bhatti, W., Bouma, L. G., & Wallace, J. 2018, astrobase

Bouma, L. G., Hartman, J. D., Bhatti, W., Winn, J. N., & Bakos, G. A. 2019, ApJS, 245, 13

Brasseur, C. E., Phillip, C., Fleming, S. W., Mullally, S. E., & White, R. L. 2019, Astrophysics Source Code Library, ascl:1905.007

Bryson, S. T., Jenkins, J. M., Gilliland, R. L., et al. 2013, Publications of the Astronomical Society of the Pacific, 125, 889

Cantat-Gaudin, T., Jordi, C., Vallenari, A., et al. 2018, Astronomy & Astrophysics, 618, A93

Eilers, P. H. C., & Marx, B. D. 1996, Statistical Science, 11, 89

Green, G. M., Schlafly, E. F., Finkbeiner, D., et al. 2018, Monthly Notices of the Royal Astronomical Society, 478, 651

Hippke, M., David, T. J., Mulders, G. D., & Heller, R. 2019, arXiv:1906.00966 [astro-ph], arXiv: 1906.00966

Hippke, M., & Heller, R. 2019, arXiv:1901.02015 [astro-ph], arXiv: 1901.02015

Huang, C. X., Burt, J., Vanderburg, A., et al. 2018, The Astrophysical Journal, 868, L39

Jenkins, J. M., Caldwell, D. A., Chandrasekaran, H., et al. 2010, The Astrophysical Journal Letters, 713, L87

Katz, D., Sartoretti, P., Cropper, M., et al. 2019, Astronomy & Astrophysics, 622, A205

Kharchenko, N. V., Piskunov, A. E., Schilbach, E., Röser, S., & Scholz, R.-D. 2013, Astronomy and Astrophysics, 558, A53

Kostov, V. B., Schlieder, J. E., Barclay, T., et al. 2019, arXiv:1903.08017 [astro-ph], arXiv: 1903.08017

Kounkel, M., & Covey, K. 2019, The Astronomical Journal, 158, 122

Pecaut, M. J., & Mamajek, E. E. 2013, The Astrophysical Journal Supplement Series, 208, 9

Schlegel, D. J., Finkbeiner, D. P., & Davis, M. 1998, The Astrophysical Journal, 500, 525

Servén, D., Brummitt, C., & Abedi, H. 2018, dswah/pyGAM: v0.8.0

Stassun, K. G., Oelkers, R. J., Paegert, M., et al. 2019, arXiv:1905.10694 [astro-ph], arXiv: 1905.10694

Stellingwerf, R. F. 1978, The Astrophysical Journal, 224, 953